ACS APPLIED MATERIALS & INTERFACES

www.acsami.org

Research Article

Controlled Vapor–Liquid–Solid Growth of Long and Remarkably Thin $Pb_{1-x}Sn_xTe$ Nanowires with Strain-Tunable Ferroelectric Phase Transition

T. X. Zhang, B. Samanta, J. Wang, A. B. Georgescu, H. A. Fertig, and S. X. Zhang*

Cite This: *ACS Appl. Mater. Interfaces* 2024, 16, 54837–54846

Read Online

ACCESS | Metrics & More | Article Recommendations | Supporting Information

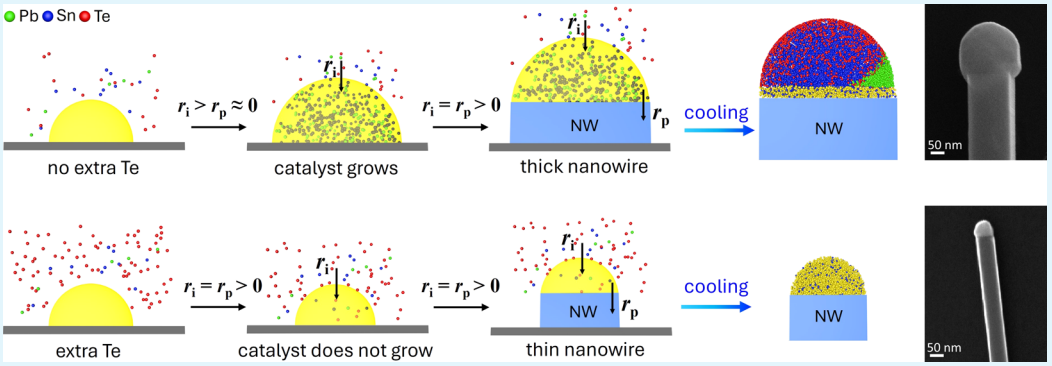

ABSTRACT: The $Pb_{1-x}Sn_xTe$ family of compounds possess a wide range of intriguing and useful physical properties, including topologically protected surface states, robust ferroelectricity, remarkable thermoelectric properties, and potential topological superconductivity. Compared to bulk crystals, one-dimensional (1D) nanowires (NWs) offer a unique platform to enhance the functional properties and enable new capabilities, e.g., to realize 1D Majorana zero modes for quantum computations. However, it has been challenging to achieve controlled synthesis of ultrathin $Pb_{1-x}Sn_xTe$ ($0 \le x \le 1$) nanowires in the truly 1D region. In this work, we report on a Au-catalyzed vapor–liquid–solid (VLS) growth of remarkably thin (20–30 nm) and sufficiently long (several to tens of micrometers) $Pb_{1-x}Sn_xTe$ nanowires of high single-crystalline quality in a controlled fashion. This controlled growth was achieved by enhancing the incorporation of Te into the Au catalyst particle to facilitate the precipitation of the Sn/Pb species and suppress the enlargement of the particle, which we identified as a major challenge for the growth of ultrathin nanowires. Our growth strategy can be easily extended to other compound and alloy nanowires, where the constituent elements have different incorporation rates into the catalyst particle. Furthermore, the growth of thin $Pb_{1-x}Sn_xTe$ nanowires enabled strain-dependent electrical transport measurements, which shows an enhancement of electrical resistance and ferroelectric transition temperature induced by uniaxial tensile strain along the nanowire axial direction, consistent with density functional theory calculations of the structural phase stability.

KEYWORDS: *topological materials, nanowires, vapor–liquid–solid growth, straintronics, ferroelectric phase transition*

I. INTRODUCTION

$Pb_{1-x}Sn_xTe$-based IV–VI compounds belong to a family of topological materials, namely, topological crystalline insulators (TCIs), which host insulating bulk (in the ideal case) and metallic surface states protected by crystal symmetries.[1−4] The topologically nontrivial electronic states with unique charge and spin properties in TCIs hold great promise for low-power electronics, spintronics, and quantum computing.[5,6] Beyond their topological surface properties, the $Pb_{1-x}Sn_xTe$ family of compounds also possess compelling ferroelectric (FE)[7,8] and thermoelectric properties[9,10] of great interest for both fundamental research and potential applications. As an example, bulk SnTe undergoes a phase transition from a paraelectric (PE) state to a FE state at a critical temperature, T_c (~100 K or below), which is accompanied by a structural phase transition from cubic ($Fm\bar{3}m$) to rhombohedral ($R3m$). There have been considerable efforts in recent years to enhance T_c for ferroelectric device applications.[7,11,12]

Nanostructuring is one of the most promising approaches to enhance the functional properties of quantum materials. In particular, nanowires (NWs) are advantageous for the study of

Received: July 11, 2024
Revised: August 23, 2024
Accepted: September 13, 2024
Published: September 28, 2024

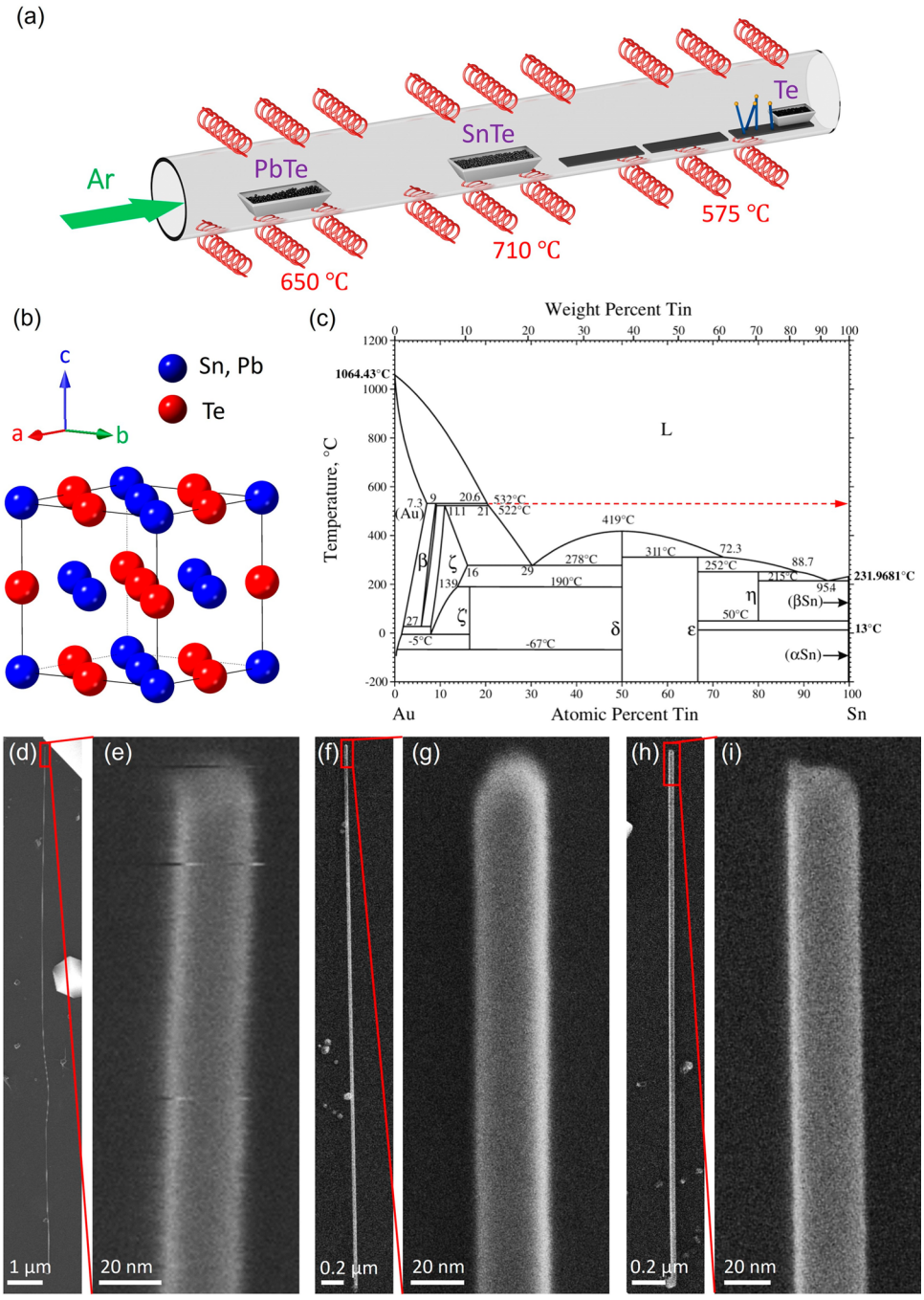

Figure 1. (a) Schematic illustration of the CVD setup used in this work. (b) Rock-salt FCC cubic crystal structure of SnTe and PbTe. (c) Au−Sn binary phase diagram. The red arrow indicates that Sn itself will never saturate in Au at the nanowire growth temperature. Reprinted with permission from ref 46. Copyright 2007 Springer Nature. Scanning electron microscopy (SEM) images at different magnifications of ultrathin (d, e) PbTe nanowire, (f, g) SnTe nanowire, and (h, i) $Pb_{1-x}Sn_xTe$ nanowire grown using 20 nm Au catalyst particles with extra Te precursor.

topological surface states because of their large surface area-to-volume ratio and enhanced surface state contributions to transport properties.[13,14] The $Pb_{1-x}Sn_xTe$ family of nanowires[15−20] also offer an excellent platform to explore one-dimensional (1D) topological superconductivity with Majorana zero modes for fault-tolerant topological quantum computation.[21,22] The 1D nanoscale geometry allows for the fabrication of wrap-around gates to achieve effective tuning of electronic states by electric gating and straintronic devices for strain engineering of electrical properties. Furthermore, topological nanowires have shown enhanced thermoelectric properties, such as increased thermopower and/or decreased thermal conductivity, in comparison to bulk samples.[23,24]

To exploit the attractive properties described above, it is essential to develop synthetic approaches to grow single-crystalline nanowires with high aspect ratios (i.e., large length to diameter ratio) in a precisely controlled fashion. To date, the $Pb_{1-x}Sn_xTe$ family of nanowires have been grown by chemical vapor deposition (CVD)[14,23,25−36] and molecule beam epitaxy (MBE),[20,37−39] mostly via an Au-catalyzed vapor−liquid−solid (VLS) process. In an ideal VLS growth, the nanowire diameter is nearly identical to the size of the

https://doi.org/10.1021/acsami.4c11537
ACS Appl. Mater. Interfaces 2024, 16, 54837−54846

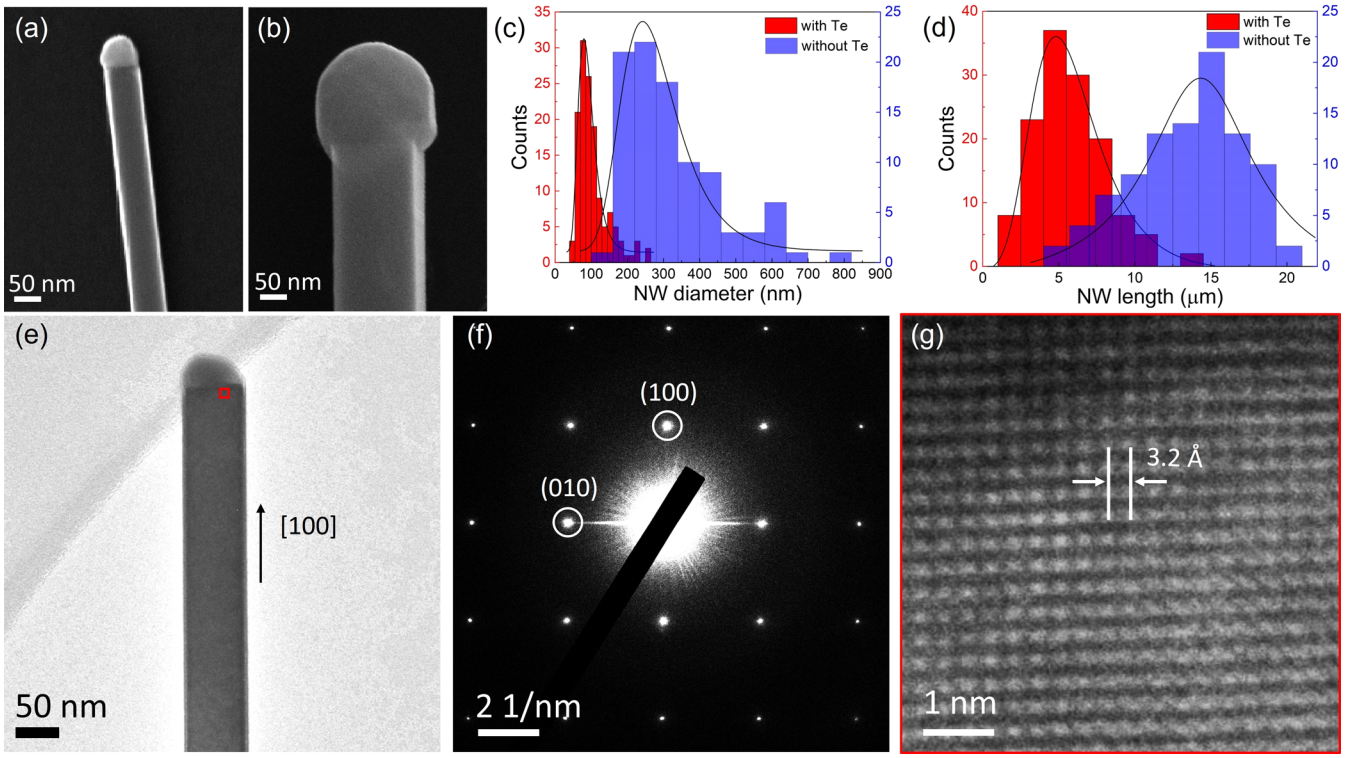

Figure 2. SEM images of two representative thin $Pb_{1-x}Sn_xTe$ nanowires grown using 50 nm Au catalysts (a) with and (b) without extra Te precursor. Histograms of $Pb_{1-x}Sn_xTe$ nanowire (c) diameters and (d) lengths with (red) and without (blue) extra Te, in which the columns correspond to the *y*-axis labels in the same color. (e) Low-magnification transmission electron microscopy (TEM) image of a thin $Pb_{1-x}Sn_xTe$ nanowire with extra Te precursor and (f) the corresponding selected-area electron diffraction (SAED) pattern. (g) High-resolution TEM (HRTEM) image obtained in the area indicated by the red square in (e).

catalyst particles, as seen in the growth of elemental nanowires.[40,41] However, with a broad distribution, the average diameters of the $Pb_{1-x}Sn_xTe$-based nanowires were reported to be significantly larger than the *initial* diameter of the Au nanoparticles, in spite of the correlation between the two scales.[23,25−28,37] By replacing Au with Au−Sn−Te alloy particles as catalysts, Liu et al. have recently reduced the average diameter of the SnTe nanowires by a factor of 3, down to the size of the alloy particles (~85 nm).[42] The length of these nanowires, however, decreases proportionally, yielding a nearly identical aspect ratio between the Au- and alloy-catalyzed wires. In a recent catalyst-free growth of $Pb_{1-x}Sn_xTe$ nanowires using MBE, Mientjes et al. have tuned the nanowire aspect ratio by a factor of 4 through a systematic tailoring of the growth parameters.[43] These MBE-grown nanowires are typically hundreds of nanometers thick and ~2 μm long. Reducing the diameter down to a few tens of nanometers (while still maintaining lengths above several microns) in a controlled fashion will not only enable the study of confinement effects on the topological, thermoelectric, and ferroelectric properties but also facilitate the engineering of these properties, by means of strain engineering and/or electric gating.

In this work, we have identified the enlargement of catalyst particles as a major challenge in the VLS growth of ultrathin compound nanowires. By addressing this challenge, we have achieved single-crystalline, remarkably thin $Pb_{1-x}Sn_xTe$ nanowires, down to the 20−30 nm regime with a length from a few to tens of microns. Strain-dependent electrical transport studies were carried out on the as-grown thin nanowires using a three-point bending method, where we observed an enhancement of the ferroelectric transition temperature under uniaxial tensile strain, consistent with our density functional theory (DFT) calculations of the structural phase stability.

II. RESULTS AND DISCUSSION

As shown in Figure 1b, SnTe and PbTe share the same rock-salt face-centered cubic (FCC) structure with a space group of $Fm\bar{3}m$. Their similar lattice constants allow for the formation of $Pb_xSn_{1-x}Te$ solid solutions with x ranging from 0 to 1.[4,28,44,45] In the previous VLS growth of SnTe (or PbTe) nanowires using Au nanoparticles as catalysts, the size of the catalyst particles after the growth often becomes several times larger than its initial value.[23−25,37,42] The nanowire diameter is nearly identical to or larger than the final size of the particle. As a result, the as-grown nanowires are typically on the order of a hundred nanometers thick even though the Au particles were initially as small as 20 nm.[23−25,42] Here, we argue that the enlargement of the catalyst particles during nanowire growth can be understood based on the Au−Sn and Au−Pb binary phase diagrams shown in Figures 1c and S1.[46,47] Using the Au−Sn phase diagram as an example, when sufficient Sn (e.g., 22% at ~530 °C) is dissolved into the Au particle, it forms an Au−Sn alloy droplet (or liquid particle). In the extreme case where no Te is present, any further feeding of Sn into the liquid particle will increase only its size but not cause any precipitation of Sn into a solid phase to form a nanowire, as long as the temperature is above ~419 °C (which is typical in the SnTe nanowire growth). To minimize the enlargement of the particle, sufficient Te must be introduced, which facilitates the precipitation of Sn by forming solid SnTe. The Pb−Au phase diagram is qualitatively similar; therefore, the same

https://doi.org/10.1021/acsami.4c11537
ACS Appl. Mater. Interfaces 2024, 16, 54837−54846

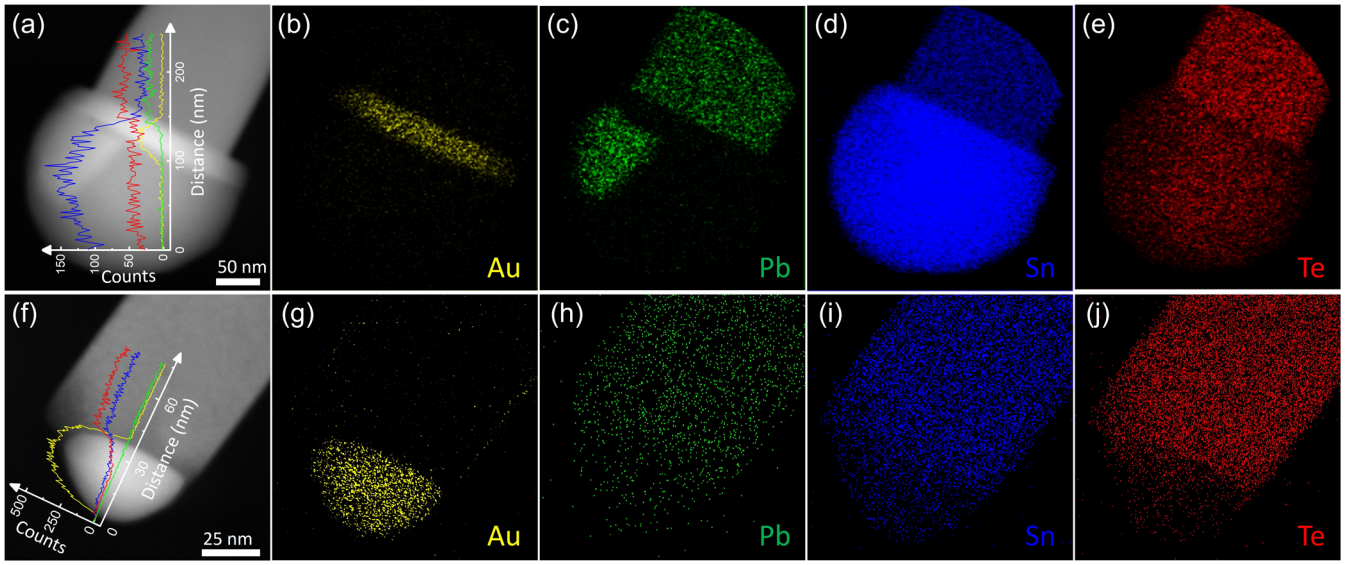

Figure 3. Scanning transmission electron microscopy (STEM) images and EDS mappings near the droplets of $Pb_{1-x}Sn_xTe$ nanowires (a–e) without and (f–j) with the presence of additional Te source. The corresponding EDS line scan data are superimposed in (a, f), where the data were taken along the distance axis. The lines in yellow, green, blue, and red colors represent Au, Pb, Sn, and Te, respectively. EDS mapping (b–e) was conducted in a circular region.

argument applies to the growth of $Pb_xSn_{1-x}Te$ nanowires. The observed enlargement of particles and detection of a large amount of Sn or Pb, but barely any Te in the catalyst particle suggests that the Te supply was not sufficient in most of the previous growths.[20,23−25,28,29,37,48]

Based on the above rationale, we added extra Te powder into the CVD reactor (see experimental details and Figure 1a) to provide sufficient incorporation of Te into the Au particle for controlled growth of thin $Pb_xSn_{1-x}Te$ ($0 \leq x \leq 1$) nanowires. Indeed, as shown in Figure 1d–i, we have achieved thin nanowires that have diameters of about 20–30 nm, close to the initial size (20 nm) of the Au particles, and lengths from several micrometers to tens of micrometers, suitable for nanodevice fabrication. The aspect ratios of these thin wires are therefore calculated to be in a range of 100–1000. To demonstrate the critical role of the additional Te, we compare the growth results with and without Te. Figure 2a,b shows scanning electron microscopy (SEM) images of the two representative thin $Pb_xSn_{1-x}Te$ nanowires grown using 50 nm Au with and without extra Te, respectively. The 50 nm Au was chosen to visualize the catalyst/alloy particles more clearly in the SEM images. The size of the catalyst particle after the growth is nearly the same as the nanowire diameter for both cases, indicating negligible vapor–solid deposition on the nanowire surface. The use of an extra Te source reduces the nanowire diameter and the particle size from ∼170 to ∼60 nm. It is worth mentioning that the catalyst particles have a hemisphere-like shape after the growth. This geometric transformation from a spherical particle to a hemisphere shape increases its diameter from 50 nm to $\sqrt[3]{2} \times 50 = 63$ nm. The fact that the diameter of the hemispherical particle at the tip of the thinner nanowire is close to 63 nm (Figure 2a) suggests that the particle must contain mainly Au. On the other hand, Au must be only a small fraction in concentration in the larger particle at the tip of the thicker nanowire shown in Figure 2b. As will be discussed later, this reasoning is indeed supported by chemical compositional characterizations.

To statistically demonstrate the importance of extra Te precursors in producing thin nanowires, we have measured the dimensions of a large number of nanowires from the two growths. As shown in Figure 2c, the nanowire diameters have evidently shifted from an average value of 326 ± 134 nm (median 295 nm) to 103 ± 42 nm (median 93 nm) when extra Te is added to the growth. While the thicker nanowires in general have longer lengths (∼13.5 μm on average) than the thinner wires (∼6.4 μm), as shown in Figure 2d, the latter has a higher aspect ratio than the former (∼74 vs ∼48), unlike in the alloy-catalyzed growth where the length shrinks proportionally with diameter.[42] It is also important to note that the thinner wires are still adequately long for device fabrication and transport measurements. The slightly shorter length in the thinner wires is attributed to the Gibbs–Thomson (GT) effect, in the sense that the growth rate is decreased as the catalyst particle size is reduced, a phenomenon widely observed in the VLS growth of nanowires.[49−52] Furthermore, pure PbTe and SnTe nanowires grown with and without extra Te source were compared in Supporting Information Section 2, which confirms that an extra supply of Te precursor promotes thinner nanowire growth in the undoped cases as well.

Transmission electron microscopy (TEM) studies were carried out to characterize the crystalline quality of the as-grown $Pb_xSn_{1-x}Te$ ($0 \leq x \leq 1$) nanowires. Figure 2e–g shows the low-magnification TEM image, selected-area electron diffraction (SAED), and high-resolution TEM (HRTEM) image of a thin nanowire grown with additional Te precursor. TEM data taken on a thick nanowire without extra Te are presented in Supporting Information Section 3. The clear diffraction patterns and HRTEM images confirm the single-crystalline nature of the nanowires with an $Fm\bar{3}m$ FCC crystal structure. Both the thin and thick wires grow along the [100] direction. Similar results were observed in pure PbTe and SnTe nanowires, which are all single-crystalline and grown along [100], regardless of whether extra Te precursor was supplied. We therefore conclude that adding extra Te to the nanowire growth reduces the diameter and increases the aspect

https://doi.org/10.1021/acsami.4c11537
ACS Appl. Mater. Interfaces 2024, 16, 54837−54846

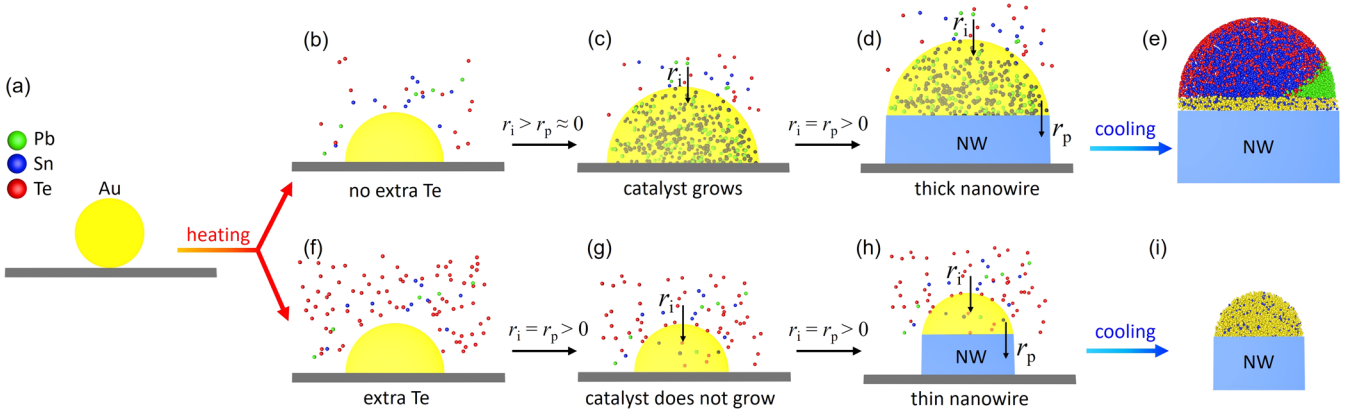

Figure 4. Schematic diagrams illustrating the influence of Te supply on the diameter of the nanowire: (a) Spherical Au catalyst nanoparticle on a substrate. (b) Pb, Sn, and Te vapor species are introduced (by heating up PbTe and SnTe powder precursor) and incorporated into Au to form liquid alloy droplet/particle. (c) The alloy particle grows larger without precipitation of species underneath it. (d) At a critical particle diameter, Pb, Sn, and Te precipitate at the same rate as they are incorporated, forming a uniform nanowire with a large diameter close to the size of the alloy particle. (e) The alloy particle solidifies upon cooling and forms separate solid phases of Au_xSn, Sn, SnTe, and Pb. (f) Extra Te vapor species is supplied by adding Te precursor to the CVD reactor. (g) The Pb, Sn, and Te species precipitate as fast as they are incorporated from the beginning, preventing the growth of the Au catalyst particle. (h) Growth of a thin nanowire with its diameter close to the initial size of the catalyst particle. (i) The alloy particle solidifies upon cooling with high concentration of Au and negligible Pb, Sn, and Te.

ratio of the nanowires while preserving the high crystalline quality and growth orientation.

To understand the underlying mechanism of the Te-promoted thinner wire growth, energy-dispersive X-ray spectroscopy (EDS) experiments were conducted on both thin and thick $Pb_xSn_{1-x}Te$ nanowires grown with and without extra Te, respectively. EDS mapping suggests that both nanowires have a uniform distribution of Pb, Sn, and Te in their bodies (Figure 3); however, quantitative analysis of EDS spectra (Figure S5) shows that the thicker wire has a Pb:Sn ratio of about 1:2 while the thinner one is about 1:8. Both nanowires have nearly the same (Pb + Sn):Te ratios of ~1:1. More importantly, the alloy particles at their tips exhibit completely distinct distributions of the chemical elements. In the case of the thicker wire, Au is present only at the interface between the particle and the nanowire. The particle itself is mostly Sn, with a small portion containing Pb that is separated from Sn. The significant amount of Sn in the particle explains why the final particle size is several times larger than its initial size before the growth. Unlike Au, Sn, and Pb, Te is evenly distributed over the entire particle, despite its relatively weaker signal. The same elemental distribution was also observed in other thicker nanowires, as shown in Figure S6. The particle at the tip of the thinner wire after growth is only slightly larger than its initial diameter of 50 nm; thus, it must mainly consist of Au, as we discussed before. This can be seen clearly in the EDS mappings, where Au shows the strongest signal. More quantitatively, the EDS spectrum shows that the particle is composed of ~90% Au and ~10% Sn with negligible amounts of Pb and Te.

In previous growth of $Pb_xSn_{1-x}Te$ nanowires, it has been widely accepted that Sn and Pb undergo a VLS process, i.e., they are incorporated into liquid Au and precipitate at the liquid–solid interface.[20,23−29,36,37,42] Whether Te follows the same pathway or enters at the vapor–liquid–solid three-phase boundary is less conclusive.[20,29,37,42,53] However, a careful examination of the Au–Te phase diagram shows that similar to Pb and Sn, Te is also soluble in liquid Au at our growth temperature (~530 °C). Moreover, the observation of Te in the particle region with relatively uniform distribution (Figure 3j) suggests that Te must be incorporated into the Au liquid particle instead of entering at the three-phase boundary. Therefore, we attribute the growth of $Pb_xSn_{1-x}Te$ nanowires to a standard VLS process, where all three elements are accommodated in the liquid Au and precipitate underneath it, forming nanowires. The wire diameter in such a VLS growth is controlled by the size of the liquid particle, which is dependent on two factors: (1) the incorporation rate r_i of the precursor species (i.e., Pb, Sn, and Te) into the liquid particle at the vapor–liquid interface; (2) the precipitation rate r_p of the species at the liquid–solid interface. If $r_p < r_i$, i.e., the species in the liquid particle are consumed slower than they are supplied from the vapor phase, and the size of the particle will grow larger. Since the solubility of Sn/Pb in Au is 100% at the growth temperature (~530 °C), the particle size will continue to increase until r_p approaches r_i. When $r_p = r_i$, i.e., the species in the particle are consumed as fast as they are supplied, and the size of the particle will remain the same.

Figure 4 illustrates how the Te content influences the Au-catalyzed VLS growth of the nanowires. Without extra Te powder in the CVD reactor, the Te atoms incorporated into the Au liquid particle are considered to be insufficient, in comparison to Sn and Pb, although the PbTe and SnTe precursors have a ratio of (Pb + Sn): Te = 1:1. This is evidenced by the considerably lower Te concentration than that of (Pb + Sn) in the Au particle (Figure 3) and can be understood based on the GT effect. In brief, the vapor pressure $[p(d)]$ of each species in the Au particle increases as the diameter (d_{Au}) of the particle decreases[49−51]

$$p(d) = p(\infty)e^{4\sigma\Omega/d_{Au}k_BT}$$

where $p(\infty)$ is the vapor pressure of the species in bulk Au, σ is the surface energy density of Au, Ω is the atomic volume of the species, and k_BT is the thermal energy. Since the atomic volume of Te (Ω_{Te}) is the largest among the three species,[54] its vapor pressure increases more rapidly as the diameter of Au decreases (i.e., its GT effect is the most prominent). As a result, the incorporation rate of Te is the lowest among the three in the ultrasmall Au nanoparticles. With insufficient Te in

https://doi.org/10.1021/acsami.4c11537
ACS Appl. Mater. Interfaces 2024, 16, 54837−54846

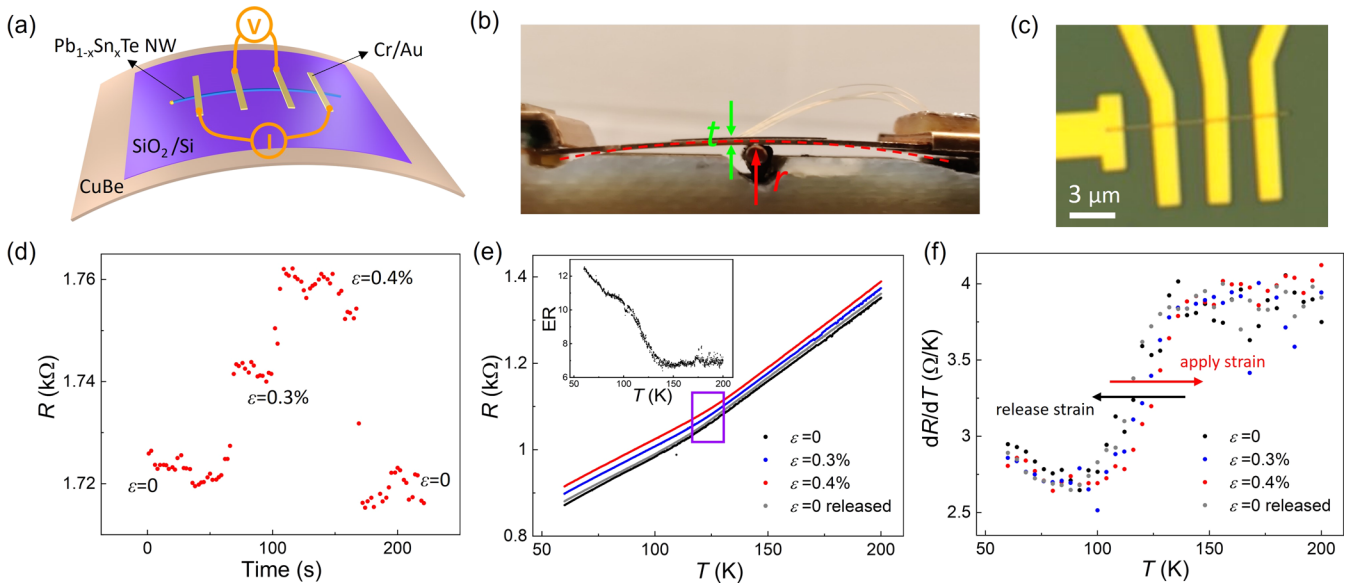

Figure 5. (a) Schematic picture of a flexible four-terminal device with a bent $Pb_{1-x}Sn_xTe$ nanowire on thin SiO_2/Si substrate and beryllium copper beam. (b) Photograph of an actual bent device. The applied strain is estimated by $\varepsilon = t/(2r)$, where t = 360 μm and r is the radius of curvature not drawn to scale. (c) Optical image of the measured four-terminal nanowire device (width ~ 78 nm, thickness ~ 90 nm). The uniaxial tensile strain is along the horizontal direction which is nearly along the nanowire axial direction with an offset of 4°, which has a negligible influence as cos4° ≈ 0.998. (d) Response of the nanowire resistance to strain at 290 K. (e) Temperature dependence of the resistance from 60 to 200 K with different uniaxial tensile strains. The inset shows the elastoresistance derived from the data with zero and 0.4% strain. (f) Derivatives of resistance with respect to temperature at a step of about 4 K.

Au, the Sn and Pb precipitate slower than they are incorporated, i.e., r_p(Sn + Pb) < r_i(Sn + Pb), which gives rise to an enlargement of the alloy particle (Figure 4b,c). As the particle grows (i.e., d_{Au} increases), the vapor pressure of Te decreases rapidly, and its incorporation rate increases, promoting the precipitation of Pb and Sn. Eventually, the system reaches an equilibrium with r_p(Sn + Pb) = r_i(Sn + Pb), where the particle size stops increasing, and the constant precipitation of Sn, Pb, and Te underneath the particle leads to the growth of a thick nanowire with a uniform diameter (Figure 4d). At the growth temperature (~530 °C), the liquid alloy particle consists of Sn, Pb, Te, and Au with different concentrations. In particular, the Sn concentration is higher than that of Pb in our specific growth, since there is more Sn than Pb vapor species due to the lower melting point of SnTe, higher precursor temperature, and shorter distance from the SnTe precursor. Upon cooling after nanowire growth, the liquid particle solidifies into separate phases of solid Pb, Sn, SnTe, and Au_xSn (Figure 4e), as revealed by EDS elemental mapping (Figure 3b−e).

With extra Te precursor added to the growth, the partial pressure of Te in the CVD reactor is dramatically increased (Figure 4f), which causes more Te atoms to incorporate into the Au (Figure 4g), facilitating the precipitation of Pb and Sn (Figure 4h). In other words, r_p(Sn + Pb) is enhanced toward the value of r_i(Sn + Pb) as the partial pressure of Te in the CVD reactor is increased to overcome its high vapor pressure in Au. In the extreme case where r_p(Sn + Pb) ≈ r_i(Sn + Pb) immediately after the VLS process starts, the catalyst particle barely increases in size, and its composition is dominated by Au along with only a low concentration of Pb, Sn, and Te (Figure 4i), as evidenced by the EDS result (Figure 3g−j). In this case, the nanowire diameter is only slightly larger than the size of the original Au particle, mainly due to the change of the particle shape from sphere to nearly hemisphere upon melting. We note that the thin nanowires grown with extra Te precursor typically contain a higher Sn:Pb ratio than the thick wires grown without additional Te, which suggests that the influence of Te on the precipitation of Sn is more dramatic than that of Pb. Additionally, the relative incorporation of Sn into the alloy particle may also be enhanced with the decrease of diameter, as observed in other Sn-based alloy nanostructures, such as SnGe.[55]

Using thin $Pb_{1-x}Sn_xTe$ (x ≈ 0.9) nanowires grown with extra Te, we fabricated nanodevices on a flexible SiO_2/Si substrate for strain-dependent transport studies. As shown in Figure 5a,b, uniaxial tensile strain was applied along the nanowire axial direction via a mechanical bending method.[56−65] The magnitude of the strain is calculated using $\varepsilon = t/(2r)$,[57] where t is the thickness measured from the top of the SiO_2/Si substrate to the bottom of the CuBe beam and r is the radius of curvature caused by bending. We first measured the strain-dependent resistance at 290 K. As shown in Figure 5d, the resistance of the nanowire is increased by 2.3% (1.2%) with an application of 0.4% (0.3%) uniaxial tensile strain, and it returns to the original value as soon as the strain is released, indicating no induced residual strain. We note that when the tensile strain is applied, the nanowire is stretched along the axial direction and presumably compressed in the cross-sectional plane so that this geometric change technically will also increase the resistance of the nanowire. However, using the Poisson's ratio of SnTe ~0.33 for an estimate,[66] we find that the geometric effect of 0.4% tensile strain can only induce a 0.67% increase in the resistance, which indicates the 2.3% increase must result mainly from the strain-induced intrinsic change in the electrical transport properties.

Figure 5e shows the resistance of the $Pb_{1-x}Sn_xTe$ (x ≈ 0.9) nanowire as a function of temperature from 200 K down to 60 K with applied strains of 0, 0.3, and 0.4%. The nanowire exhibits a typical metallic behavior, similar to previous studies

https://doi.org/10.1021/acsami.4c11537
ACS Appl. Mater. Interfaces 2024, 16, 54837−54846

of SnTe and $Pb_{1-x}Sn_xTe$ nanowires and thin films.[28,36,42,67] Tensile strain increases the resistance across the entire temperature range. The *R*-*T* curve with zero strain is well reproduced after the strain is released; this again proves that the large change in resistance is indeed a strain-induced effect instead of experimental artifacts caused by thermal cycling or the strain loading process. The inset shows the elastoresistance (ER) calculated using the data of zero and 0.4% strain, where ER is defined as $\mathrm{ER} = \frac{[R(\varepsilon) - R(0)]\,/\,R(0)}{\varepsilon}$. As the temperature decreases below ∼130 K, the ER starts to increase rapidly down to 60 K, where its value is nearly doubled in comparison to 200 K. The derivative dR/dT as a function of T shows an abrupt change at about 130 K (Figure 5f), similar to what was found in SnTe nanowires.[24,42] The abrupt change of dR/dT was attributed to a well-known ferroelectric phase transition from a cubic structure ($Fm\bar{3}m$) to rhombohedral ($R3m$) phase, as demonstrated by correlated TEM studies.[42] The rapid increase of ER at low temperatures may indicate that the electrical properties of the $Pb_{1-x}Sn_xTe$ nanowire are more sensitive to strain when it is in the rhombohedral FE phase than those in the cubic PE phase. To investigate the effect of strain on the ferroelectric phase transition temperature T_c, derivatives dR/dT as a function of temperature under different strains are compared in Figure 5f. The T_c, revealed by the sudden decrease of dR/dT,[42] shifts toward higher temperatures as more tensile strain is applied. Quantitatively, the midpoint of the abruptly changing window increases from about 118 K at zero strain to ∼122 K at 0.3% tensile strain and finally to ∼126 K at 0.4% strain. Like the resistance, the dR/dT curve also essentially returns to its original value when strain is released, which again rules out the existence of residual strain or other artifacts in the measurement. Figure S8 shows similar data in another nanowire device, again confirming the reproducibility of the results.

The ferroelectric transition temperature T_c in SnTe increases as the charge carrier density decreases.[68] Since the resistance increases as tensile strain is applied, one possibility is that the carrier density is decreased by strain, which leads to an increase of T_c. Another possibility is that the energy difference between the PE ($Fm\bar{3}m$) and FE ($R3m$) structures increases under tensile strain, causing the transition to occur at a higher temperature. To verify this possibility, we carried out strain-dependent calculations by DFT. Given the low Pb content in our nanowire, we calculated the structure energy of SnTe in the PE and FE phases. Strains up to 4% were imposed as detailed in the Experimental and Calculational Details section. As shown in Figure 6, the energy of the PE phase is always higher than that of the FE phase, meaning that the FE phase is favored at low temperatures as the DFT calculation is conducted at 0 K. This agrees with the experimental result that the PE phase at room temperature transforms to the FE phase at a low temperature T_c. The energy difference between the two phases shows a clear increasing trend with tensile strain, which may be responsible for the enhanced transition temperature.

III. CONCLUSIONS

In conclusion, we have demonstrated that a major challenge in the VLS growth of ultrathin PbSnTe nanowires relies on the enlargement of catalyst particles, which is caused by the natural Te deficiency in the particles and hence limited precipitation rates of Sn/Pb. By increasing the supply of Te in the CVD reactor, we have successfully suppressed the particle growth and achieved nanowires as thin as 20−30 nm and at least several micrometers long, suitable for device fabrication and transport studies. Our strategy can be extended/generalized to the controlled VLS growth of other compound/alloy nanowires, where precursors have imbalanced incorporation rates in the catalyst particles. Furthermore, we have observed strain-dependent electrical transport properties of the as-grown thin nanowires, where both the electrical resistance and the ferroelectric phase transition temperature are enhanced by uniaxial tensile strain along the nanowire axial direction, consistent with DFT calculations of the structural phase stabilities.

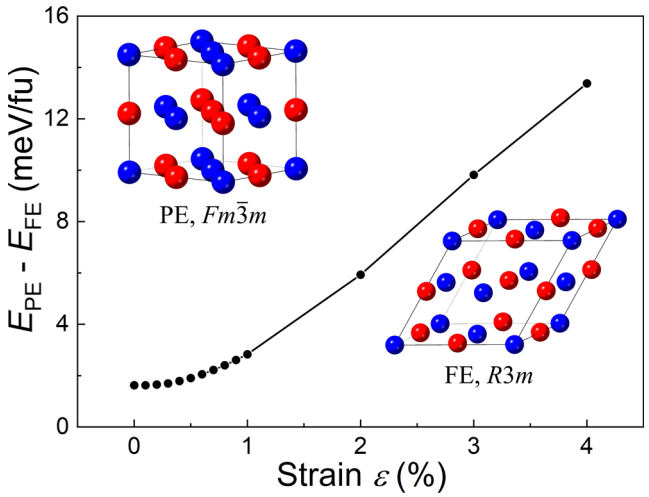

Figure 6. Calculated energy difference per formula unit between the PE and FE structures as a function of uniaxial tensile strain. Insets are the illustrations of the two structures, where the distortion of the $R3m$ structure is exaggerated for illustrative purposes.

IV. EXPERIMENTAL AND CALCULATIONAL DETAILS

IV.I. Nanowire Growth. All of our nanowires were grown in a three-zone quartz tube furnace via a VLS mechanism (Figure 1a). For the growth of $Pb_{1-x}Sn_xTe$ nanowire, lead telluride (PbTe) powder (Alfa Aesar, purity 99.999%) and tin telluride (SnTe) powder (Alfa Aesar, purity 99.999%) were placed in two alumina boats located in the centers of zone 1 and zone 2, respectively. Three silicon substrates, each ∼3 in. in length, were placed one after another from ∼4 to ∼13 in. away from the center of zone 2. All three substrates were coated with poly-L-lysine solution (Ted Pella, 0.1%) and gold colloid (Ted Pella, 20 or 50 nm) before being placed in a quartz tube. An additional tellurium source was supplied by placing a boat of Te powder (Alfa Aesar, purity 99.999%) on the third substrate, which is approximately 12 in. away from the center of zone 2. During the growth, Ar gas was flowed through the quartz tube at a rate of 10 sccm, and the pressure was kept at 30 Torr until the cooling down process. Temperatures in the three zones were heated up to 650, 710, and 575 °C in 20 min and maintained for 30 min. The nanowires were found on the third substrate approximately 11 in. away from the center of zone 2, where the temperature was ∼530 °C. For the growth of undoped SnTe (or PbTe) nanowires, SnTe (or PbTe) powder was placed at the center of both zone 1 and zone 2 or only zone 2, and all other conditions were kept the same as for the doped/alloyed nanowire growth.

IV.II. Characterizations. The morphologies and diameters of the nanowires were characterized by SEM (Quanta FEI or Zeiss Auriga 60). Since the facets of the ultra-thin nanowires could not be clearly identified in SEM, all the nanowire diameters were measured from their projection in the SEM images. The crystalline quality and

https://doi.org/10.1021/acsami.4c11537
ACS Appl. Mater. Interfaces 2024, 16, 54837−54846

growth orientations were characterized via SAED (JEOL JEM 1400plus) and HRTEM (JEOL JEM 3200FS). The chemical composition of the nanowires was determined using EDS in SEM and TEM (JEOL JEM 3200FS). The thickness of the nanowire on the device substrate was measured by atomic force microscopy (AFM, Asylum Research MFP-3D).

IV.III. Straintronic Nanodevice Fabrication and Measurements. Pads of Cr/Au (10/90 nm) were patterned onto a pristine flexible SiO_2/Si (300 nm/50 μm) substrate by using optical lithography and thermal evaporation. The SiO_2/Si substrate was then firmly attached to a nonmagnetic beryllium copper (CuBe) beam with cryogenic epoxy.[65] $Pb_{1-x}Sn_xTe$ nanowires were mechanically transferred to the substrate's center using polydimethylsiloxane (PDMS). Four-terminal resistance was measured by four Cr/Au electrodes with a thickness of ∼210 nm (fabricated by e-beam lithography), which can also avoid potential slipping of the nanowire upon bending.[59,62,63] Prior to metal evaporation, plasma cleaning and HCl etching were performed to remove any potential organic residues and surface oxides. Uniaxial tensile strain was applied using a three-point bending apparatus, and temperature-dependent resistance measurements were carried out using a partially home-built system integrated with the Quantum Design-Magnetic Property Measurement System (MPMS). More details about the application of strain and resistance measurements were described in our previous work.[65,69] Resistance values at the same temperatures were averaged. To calculate the elastoresistance, resistance data points under different strains within a temperature difference of less than 0.06 K were used. The derivatives of resistance with respect to temperature were calculated by using data points at a step of about 4 K.

IV.IV. Density Functional Theory Calculations. DFT calculations were conducted utilizing the projected augmented plane-wave (PAW) pseudopotentials, implemented in the Quantum Espresso software.[70] The Perdew−Burke−Ernzerhof (PBE) generalized gradient approximation (GGA) was employed to include the exchange-correlation interactions among the electrons. The k-mesh used was 6 × 6 × 6, and the energy cutoff was set to 680 eV. 0.0001 atomic unit was set for the convergence criteria of atomic forces. 8-atom conventional unit cells were used for both the cubic paraelectric ($Fm\bar{3}m$) and rhombohedral ferroelectric ($R3m$) structures. The optimized cubic structure has a lattice constant a = 6.405 Å; the rhombohedral structure has a = 6.419 Å and α = 89.649° with a Te atomic displacement of 0.013 (in fractional units). Strain was imposed by extending the z-direction crystal lattice vector while compressing it along x, y using the Poisson's ratio ν = 0.33 reported in ref 66.

■ ASSOCIATED CONTENT

Supporting Information

The Supporting Information is available free of charge at https://pubs.acs.org/doi/10.1021/acsami.4c11537.

Au−Pb phase diagram, SEM and TEM data of SnTe and PbTe nanowires, TEM data of thick $Pb_{1-x}Sn_xTe$ nanowires, EDS spectra, additional EDS mappings of thick $Pb_{1-x}Sn_xTe$ nanowires, nonuniform evolution of the nanowire diameter, additional strain-dependent transport data, and additional DFT calculations (PDF)

■ AUTHOR INFORMATION

Corresponding Author

S. X. Zhang − *Department of Physics, Indiana University, Bloomington, Indiana 47405, United States; Quantum Science and Engineering Center, Indiana University, Bloomington, Indiana 47405, United States;* orcid.org/0000-0002-1004-0597; Email: sxzhang@indiana.edu

Authors

T. X. Zhang − *Department of Physics, Indiana University, Bloomington, Indiana 47405, United States*

B. Samanta − *Department of Chemistry, Indiana University, Bloomington, Indiana 47405, United States*

J. Wang − *Department of Mechanical and Materials Engineering, University of Nebraska, Lincoln, Nebraska 68588, United States;* orcid.org/0000-0001-5130-300X

A. B. Georgescu − *Department of Chemistry and Quantum Science and Engineering Center, Indiana University, Bloomington, Indiana 47405, United States;* orcid.org/0000-0002-3161-1491

H. A. Fertig − *Department of Physics, Indiana University, Bloomington, Indiana 47405, United States; Quantum Science and Engineering Center, Indiana University, Bloomington, Indiana 47405, United States*

Complete contact information is available at: https://pubs.acs.org/10.1021/acsami.4c11537

Author Contributions

The manuscript was written through contributions of all authors. All authors have given approval to the final version of the manuscript.

Notes

The authors declare no competing financial interest.

■ ACKNOWLEDGMENTS

The authors acknowledge support from the U.S. National Science Foundation through grant nos. ECCS-1936406 and DMR- 1914451. They thank the Indiana University-Bloomington Nanoscale Characterization Facility for access to the characterization and device fabrication tools and Electron Microscopy Center for access to the transmission electron microscope. They also thank J. Hong for help with DFT calculations and M. Hosek for assistance with the strain apparatus. This material is also partially based upon work supported by the Industry-University Cooperative Research Center Program at the U.S. National Science Foundation under grant no. 2224928. This research was supported in part by Lilly Endowment, Inc., through its support for the Indiana University Pervasive Technology Institute.

■ REFERENCES

(1) Fu, L. Topological Crystalline Insulators. *Phys. Rev. Lett.* **2011**, *106* (10), No. 106802.

(2) Hsieh, T. H.; Lin, H.; Liu, J.; Duan, W.; Bansil, A.; Fu, L. Topological Crystalline Insulators in the SnTe Material Class. *Nat. Commun.* **2012**, *3* (1), No. 982.

(3) Tanaka, Y.; Ren, Z.; Sato, T.; Nakayama, K.; Souma, S.; Takahashi, T.; Segawa, K.; Ando, Y. Experimental Realization of a Topological Crystalline Insulator in SnTe. *Nat. Phys.* **2012**, *8* (11), 800−803.

(4) Xu, S.-Y.; Liu, C.; Alidoust, N.; Neupane, M.; Qian, D.; Belopolski, I.; Denlinger, J. D.; Wang, Y. J.; Lin, H.; Wray, L. A.; Landolt, G.; Slomski, B.; Dil, J. H.; Marcinkova, A.; Morosan, E.; Gibson, Q.; Sankar, R.; Chou, F. C.; Cava, R. J.; Bansil, A.; Hasan, M. Z. Observation of a Topological Crystalline Insulator Phase and Topological Phase Transition in $Pb_{1-x}Sn_xTe$. *Nat. Commun.* **2012**, *3* (1), No. 1192.

(5) Ando, Y.; Fu, L. Topological Crystalline Insulators and Topological Superconductors: From Concepts to Materials. *Annu. Rev. Condens. Matter Phys.* **2015**, *6*, 361−381.

(6) Hu, J.; Xu, S.-Y.; Ni, N.; Mao, Z. Transport of Topological Semimetals. *Annu. Rev. Mater. Res.* **2019**, *49*, 207−252.

(7) Chang, K.; Liu, J.; Lin, H.; Wang, N.; Zhao, K.; Zhang, A.; Jin, F.; Zhong, Y.; Hu, X.; Duan, W.; Zhang, Q.; Fu, L.; Xue, Q.-K.; Chen,

X.; Ji, S.-H. Discovery of Robust in-Plane Ferroelectricity in Atomic-Thick SnTe. *Science* **2016**, *353* (6296), 274−278.
(8) Barraza-Lopez, S.; Fregoso, B. M.; Villanova, J. W.; Parkin, S. S. P.; Chang, K. Colloquium: Physical Properties of Group-IV Monochalcogenide Monolayers. *Rev. Mod. Phys.* **2021**, *93* (1), No. 011001.
(9) Moshwan, R.; Yang, L.; Zou, J.; Chen, Z.-G. Eco-Friendly SnTe Thermoelectric Materials: Progress and Future Challenges. *Adv. Funct. Mater.* **2017**, *27* (43), No. 1703278.
(10) LaLonde, A. D.; Pei, Y.; Wang, H.; Snyder, G. J. Lead Telluride Alloy Thermoelectrics. *Mater. Today* **2011**, *14* (11), 526−532.
(11) Liu, K.; Lu, J.; Picozzi, S.; Bellaiche, L.; Xiang, H. Intrinsic Origin of Enhancement of Ferroelectricity in SnTe Ultrathin Films. *Phys. Rev. Lett.* **2018**, *121* (2), No. 027601.
(12) Chang, K.; Kaloni, T. P.; Lin, H.; Bedoya-Pinto, A.; Pandeya, A. K.; Kostanovskiy, I.; Zhao, K.; Zhong, Y.; Hu, X.; Xue, Q.-K.; Chen, X.; Ji, S.-H.; Barraza-Lopez, S.; Parkin, S. S. P. Enhanced Spontaneous Polarization in Ultrathin SnTe Films with Layered Antipolar Structure. *Adv. Mater.* **2019**, *31* (3), No. 1804428.
(13) Liu, P.; Williams, J. R.; Cha, J. J. Topological Nanomaterials. *Nat. Rev. Mater.* **2019**, *4* (7), 479−496.
(14) Liu, C.-W.; Wang, Z.; Qiu, R. L. J.; Gao, X. P. A. Development of Topological Insulator and Topological Crystalline Insulator Nanostructures. *Nanotechnology* **2020**, *31* (19), No. 192001.
(15) Nguyen, N. M.; Brzezicki, W.; Hyart, T. Corner States, Hinge States, and Majorana Modes in SnTe Nanowires. *Phys. Rev. B* **2022**, *105* (7), No. 075310.
(16) Cao, Z.; Liu, D. E.; He, W.-X.; Liu, X.; He, K.; Zhang, H. Numerical Study of PbTe-Pb Hybrid Nanowires for Engineering Majorana Zero Modes. *Phys. Rev. B* **2022**, *105* (8), No. 085424.
(17) Geng, Z.; Zhang, Z.; Chen, F.; Yang, S.; Jiang, Y.; Gao, Y.; Tong, B.; Song, W.; Miao, W.; Li, R.; Wang, Y.; Zhang, Q.; Meng, F.; Gu, L.; Zhu, K.; Zang, Y.; Li, L.; Shang, R.; Feng, X.; Xue, Q.-K.; He, K.; Zhang, H. Observation of Aharonov-Bohm Effect in PbTe Nanowire Networks. *Phys. Rev. B* **2022**, *105* (24), No. L241112.
(18) Jung, J.; Schellingerhout, S. G.; Ritter, M. F.; ten Kate, S. C.; van der Molen, O. A. H.; de Loijer, S.; Verheijen, M. A.; Riel, H.; Nichele, F.; Bakkers, E. P. A. M. Selective Area Growth of PbTe Nanowire Networks on InP. *Adv. Funct. Mater.* **2022**, *32* (51), No. 2208974.
(19) Song, W.; Wang, Y.; Miao, W.; Yu, Z.; Gao, Y.; Li, R.; Yang, S.; Chen, F.; Geng, Z.; Zhang, Z.; Zhang, S.; Zang, Y.; Cao, Z.; Liu, D. E.; Shang, R.; Feng, X.; Li, L.; Xue, Q.-K.; He, K.; Zhang, H. Conductance Quantization in PbTe Nanowires. *Phys. Rev. B* **2023**, *108* (4), No. 045426.
(20) Schellingerhout, S. G.; de Jong, E. J.; Gomanko, M.; Guan, X.; Jiang, Y.; Hoskam, M. S. M.; Jung, J.; Koelling, S.; Moutanabbir, O.; Verheijen, M. A.; Frolov, S. M.; Bakkers, E. P. A. M. Growth of PbTe Nanowires by Molecular Beam Epitaxy. *Mater. Quantum Technol.* **2022**, *2* (1), No. 015001.
(21) Mourik, V.; Zuo, K.; Frolov, S. M.; Plissard, S. R.; Bakkers, E. P. A. M.; Kouwenhoven, L. P. Signatures of Majorana Fermions in Hybrid Superconductor-Semiconductor Nanowire Devices. *Science* **2012**, *336* (6084), 1003−1007.
(22) Rokhinson, L. P.; Liu, X.; Furdyna, J. K. The Fractional A.C. Josephson Effect in a Semiconductor−Superconductor Nanowire as a Signature of Majorana Particles. *Nat. Phys.* **2012**, *8* (11), 795−799.
(23) Xu, E.; Li, Z.; Acosta, J. A.; Li, N.; Swartzentruber, B.; Zheng, S.; Sinitsyn, N.; Htoon, H.; Wang, J.; Zhang, S. Enhanced Thermoelectric Properties of Topological Crystalline Insulator PbSnTe Nanowires Grown by Vapor Transport. *Nano Res.* **2016**, *9* (3), 820−830.
(24) Xu, E. Z.; Li, Z.; Martinez, J. A.; Sinitsyn, N.; Htoon, H.; Li, N.; Swartzentruber, B.; Hollingsworth, J. A.; Wang, J.; Zhang, S. X. Diameter Dependent Thermoelectric Properties of Individual SnTe Nanowires. *Nanoscale* **2015**, *7* (7), 2869−2876.
(25) Li, Z.; Shao, S.; Li, N.; McCall, K.; Wang, J.; Zhang, S. X. Single Crystalline Nanostructures of Topological Crystalline Insulator SnTe with Distinct Facets and Morphologies. *Nano Lett.* **2013**, *13* (11), 5443−5448.
(26) Safdar, M.; Wang, Q.; Mirza, M.; Wang, Z.; He, J. Crystal Shape Engineering of Topological Crystalline Insulator SnTe Microcrystals and Nanowires with Huge Thermal Activation Energy Gap. *Cryst. Growth Des.* **2014**, *14* (5), 2502−2509.
(27) Saghir, M.; Lees, M. R.; York, S. J.; Balakrishnan, G. Synthesis and Characterization of Nanomaterials of the Topological Crystalline Insulator SnTe. *Cryst. Growth Des.* **2014**, *14* (4), 2009−2013.
(28) Safdar, M.; Wang, Q.; Wang, Z.; Zhan, X.; Xu, K.; Wang, F.; Mirza, M.; He, J. Weak Antilocalization Effect of Topological Crystalline Insulator $Pb_{1-x}Sn_xTe$ Nanowires with Tunable Composition and Distinct {100} Facets. *Nano Lett.* **2015**, *15* (4), 2485−2490.
(29) Zou, Y.; Chen, Z.; Lin, J.; Zhou, X.; Lu, W.; Drennan, J.; Zou, J. Morphological Control of SnTe Nanostructures by Tuning Catalyst Composition. *Nano Res.* **2015**, *8* (9), 3011−3019.
(30) Saghir, M.; Sanchez, A. M.; Hindmarsh, S. A.; York, S. J.; Balakrishnan, G. Nanomaterials of the Topological Crystalline Insulators, $Pb_{1-x}Sn_xTe$ and $Pb_{1-x}Sn_xSe$. *Cryst. Growth Des.* **2015**, *15* (11), 5202−5206.
(31) Zou, Y.-C.; Chen, Z.-G.; Kong, F.; Lin, J.; Drennan, J.; Cho, K.; Wang, Z.; Zou, J. Planar Vacancies in $Sn_{1-x}Bi_xTe$ Nanoribbons. *ACS Nano* **2016**, *10* (5), 5507−5515.
(32) Atherton, S.; Steele, B.; Sasaki, S. Unexpected Au Alloying in Tailoring in-Doped SnTe Nanostructures with Gold Nanoparticles. *Crystals* **2017**, *7* (3), 78.
(33) Wang, J.; Xie, D.; Li, Z.; Zhang, X.; Sun, X.; Coughlin, A. L.; Ruch, T.; Chen, Q.; Losovyj, Y.; Lee, S.; Yu, H.; Zhou, H.; Wang, H.; Wang, J.; Zhang, S. Self-Organization of Various "Phase-Separated" Nanostructures in a Single Chemical Vapor Deposition. *Nano Res.* **2020**, *13* (6), 1723−1732.
(34) Fardy, M.; Hochbaum, A. I.; Goldberger, J.; Zhang, M. M.; Yang, P. Synthesis and Thermoelectrical Characterization of Lead Chalcogenide Nanowires. *Adv. Mater.* **2007**, *19* (19), 3047−3051.
(35) Roh, J. W.; Jang, S. Y.; Kang, J.; Lee, S.; Noh, J.-S.; Kim, W.; Park, J.; Lee, W. Size-Dependent Thermal Conductivity of Individual Single-Crystalline PbTe Nanowires. *Appl. Phys. Lett.* **2010**, *96* (10), No. 103101.
(36) Safdar, M.; Wang, Q.; Mirza, M.; Wang, Z.; Xu, K.; He, J. Topological Surface Transport Properties of Single-Crystalline SnTe Nanowire. *Nano Lett.* **2013**, *13* (11), 5344−5349.
(37) Sadowski, J.; Dziawa, P.; Kaleta, A.; Kurowska, B.; Reszka, A.; Story, T.; Kret, S. Defect-Free SnTe Topological Crystalline Insulator Nanowires Grown by Molecular Beam Epitaxy on Graphene. *Nanoscale* **2018**, *10* (44), 20772−20778.
(38) Dziawa, P.; Sadowski, J.; Dluzewski, P.; Lusakowska, E.; Domukhovski, V.; Taliashvili, B.; Wojciechowski, T.; Baczewski, L. T.; Bukala, M.; Galicka, M.; Buczko, R.; Kacman, P.; Story, T. Defect Free PbTe Nanowires Grown by Molecular Beam Epitaxy on GaAs(111)B Substrates. *Cryst. Growth Des.* **2010**, *10* (1), 109−113.
(39) Volobuev, V. V.; Stetsenko, A. N.; Mateychenko, P. V.; Zubarev, E. N.; Samburskaya, T.; Dziawa, P.; Reszka, A.; Story, T.; Sipatov, A. Y. Bi Catalyzed VLS Growth of PbTe (001) Nanowires. *J. Cryst. Growth* **2011**, *318* (1), 1105−1108.
(40) Cui, Y.; Lauhon, L. J.; Gudiksen, M. S.; Wang, J.; Lieber, C. M. Diameter-Controlled Synthesis of Single-Crystal Silicon Nanowires. *Appl. Phys. Lett.* **2001**, *78* (15), 2214−2216.
(41) Wu, Y.; Cui, Y.; Huynh, L.; Barrelet, C. J.; Bell, D. C.; Lieber, C. M. Controlled Growth and Structures of Molecular-Scale Silicon Nanowires. *Nano Lett.* **2004**, *4* (3), 433−436.
(42) Liu, P.; Han, H. J.; Wei, J.; Hynek, D.; Hart, J. L.; Han, M. G.; Trimble, C. J.; Williams, J.; Zhu, Y.; Cha, J. J. Synthesis of Narrow SnTe Nanowires Using Alloy Nanoparticles. *ACS Appl. Electron. Mater.* **2021**, *3* (1), 184−191.
(43) Mientjes, M. G.; Guan, X.; Lueb, P. J.; Verheijen, M. A.; Bakkers, E. P. Catalyst-Free MBE Growth of PbSnTe Nanowires with Tunable Aspect Ratio. 2024, arXiv:2401.04990. arXiv.org e-Print archive. http://arxiv.org/abs/2401.04990.

https://doi.org/10.1021/acsami.4c11537
ACS Appl. Mater. Interfaces 2024, 16, 54837−54846

(44) Iizumi, M.; Hamaguchi, Y.; Komatsubara, K. F.; Kato, Y. Phase Transition in SnTe with Low Carrier Concentration. *J. Phys. Soc. Jpn.* **1975**, *38* (2), 443−449.
(45) Shrestha, K.; Miertschin, D.; Sankar, R.; Lorenz, B.; Chu, C. W. Large Magnetoresistance and Quantum Oscillations in $Sn_{0.05}Pb_{0.95}Te$. *J. Phys.: Condens. Matter* **2021**, *33* (33), No. 335501.
(46) Okamoto, H. Au-Sn (Gold-Tin). *J. Phase Equilib. Diffus.* **2007**, *28* (5), 490.
(47) Okamoto, H. Au-Pb (Gold-Lead). *J. Phase Equilib.* **1993**, *14* (5), 648−649.
(48) Li, Z.; Xu, E.; Losovyj, Y.; Li, N.; Chen, A.; Swartzentruber, B.; Sinitsyn, N.; Yoo, J.; Jia, Q.; Zhang, S. Surface Oxidation and Thermoelectric Properties of Indium-Doped Tin Telluride Nanowires. *Nanoscale* **2017**, *9* (35), 13014−13024.
(49) Givargizov, E. I. Fundamental Aspects of VLS Growth. *J. Cryst. Growth* **1975**, *31*, 20−30.
(50) Fröberg, L. E.; Seifert, W.; Johansson, J. Diameter-Dependent Growth Rate of InAs Nanowires. *Phys. Rev. B* **2007**, *76* (15), No. 153401.
(51) Dubrovskii, V. G.; Sibirev, N. V.; Cirlin, G. E.; Soshnikov, I. P.; Chen, W. H.; Larde, R.; Cadel, E.; Pareige, P.; Xu, T.; Grandidier, B.; Nys, J. P.; Stievenard, D.; Moewe, M.; Chuang, L. C.; Chang-Hasnain, C. Gibbs-Thomson and Diffusion-Induced Contributions to the Growth Rate of Si, InP, and GaAs Nanowires. *Phys. Rev. B* **2009**, *79* (20), No. 205316.
(52) Shen, Y.; Chen, R.; Yu, X.; Wang, Q.; Jungjohann, K. L.; Dayeh, S. A.; Wu, T. Gibbs−Thomson Effect in Planar Nanowires: Orientation and Doping Modulated Growth. *Nano Lett.* **2016**, *16* (7), 4158−4165.
(53) Song, M.; Lee, J.; Wang, B.; Legg, B. A.; Hu, S.; Chun, J.; Li, D. In situ Characterization of Kinetics and Mass Transport of PbSe Nanowire Growth via LS and VLS Mechanisms. *Nanoscale* **2019**, *11* (13), 5874−5878.
(54) Singman, C. N. Atomic Volume and Allotropy of the Elements. *J. Chem. Educ.* **1984**, *61* (2), 137.
(55) Seifner, M. S.; Biegger, F.; Lugstein, A.; Bernardi, J.; Barth, S. Microwave-Assisted $Ge_{1-x}Sn_x$ Nanowire Synthesis: Precursor Species and Growth Regimes. *Chem. Mater.* **2015**, *27* (17), 6125−6130.
(56) Atkin, J. M.; Berweger, S.; Chavez, E. K.; Raschke, M. B.; Cao, J.; Fan, W.; Wu, J. Strain and Temperature Dependence of the Insulating Phases of VO_2 near the Metal-Insulator Transition. *Phys. Rev. B* **2012**, *85* (2), No. 020101.
(57) Mohiuddin, T. M. G.; Lombardo, A.; Nair, R. R.; Bonetti, A.; Savini, G.; Jalil, R.; Bonini, N.; Basko, D. M.; Galiotis, C.; Marzari, N.; Novoselov, K. S.; Geim, A. K.; Ferrari, A. C. Uniaxial Strain in Graphene by Raman Spectroscopy: *G* Peak Splitting, Grüneisen Parameters, and Sample Orientation. *Phys. Rev. B* **2009**, *79* (20), No. 205433.
(58) He, K.; Poole, C.; Mak, K. F.; Shan, J. Experimental Demonstration of Continuous Electronic Structure Tuning via Strain in Atomically Thin MoS_2. *Nano Lett.* **2013**, *13* (6), 2931−2936.
(59) Conley, H. J.; Wang, B.; Ziegler, J. I.; Haglund, R. F., Jr.; Pantelides, S. T.; Bolotin, K. I. Bandgap Engineering of Strained Monolayer and Bilayer MoS_2. *Nano Lett.* **2013**, *13* (8), 3626−3630.
(60) Datye, I. M.; Daus, A.; Grady, R. W.; Brenner, K.; Vaziri, S.; Pop, E. Strain-Enhanced Mobility of Monolayer MoS_2. *Nano Lett.* **2022**, *22* (20), 8052−8059.
(61) Desai, S. B.; Seol, G.; Kang, J. S.; Fang, H.; Battaglia, C.; Kapadia, R.; Ager, J. W.; Guo, J.; Javey, A. Strain-Induced Indirect to Direct Bandgap Transition in Multilayer WSe_2. *Nano Lett.* **2014**, *14* (8), 4592−4597.
(62) Aslan, B.; Datye, I. M.; Mleczko, M. J.; Sze Cheung, K.; Krylyuk, S.; Bruma, A.; Kalish, I.; Davydov, A. V.; Pop, E.; Heinz, T. F. Probing the Optical Properties and Strain-Tuning of Ultrathin $Mo_{1-x}W_xTe_2$. *Nano Lett.* **2018**, *18* (4), 2485−2491.
(63) Huang, M.; Yan, H.; Heinz, T. F.; Hone, J. Probing Strain-Induced Electronic Structure Change in Graphene by Raman Spectroscopy. *Nano Lett.* **2010**, *10* (10), 4074−4079.
(64) Hu, G.; Wu, J.; Ma, C.; Liang, Z.; Liu, W.; Liu, M.; Wu, J. Z.; Jia, C.-L. Controlling the Dirac Point Voltage of Graphene by Mechanically Bending the Ferroelectric Gate of a Graphene Field Effect Transistor. *Mater. Horiz.* **2019**, *6* (2), 302−310.
(65) Zhang, T.; Hong, J.; Coughlin, A. L.; Nnokwe, C.; Hosek, M. K.; He, R.; Fertig, H. A.; Zhang, S. Anisotropic Straintronic Transport in Topological Semimetal Nanoflakes. *ACS Appl. Nano Mater.* **2024**, *7* (11), 13101−13109.
(66) Muthumari, M.; Manjula, M.; Krishnaveni, S.; Pradheepa, K. Structural, Electronic and Mechanical Properties of SnTe and Selenium Doped SnTe-Ab Initio Study. *Mater. Today: Proc.* **2022**, *50*, 2741−2744.
(67) Liu, C.-W.; Wei, F.; Premasiri, K.; Liu, S.; Ma, S.; Zhang, Z.; Gao, X. P. A. Non-Drude Magneto-Transport Behavior in a Topological Crystalline Insulator/Band Insulator Heterostructure. *Nano Lett.* **2018**, *18* (10), 6538−6543.
(68) Kobayashi, K. L. I.; Kato, Y.; Katayama, Y.; Komatsubara, K. F. Carrier-Concentration-Dependent Phase Transition in SnTe. *Phys. Rev. Lett.* **1976**, *37* (12), 772−774.
(69) Yang, W.; Coughlin, A. L.; Webster, L.; Ye, G.; Lopez, K.; Fertig, H. A.; He, R.; Yan, J.-A.; Zhang, S. Highly Tunable Raman Scattering and Transport in Layered Magnetic Cr_2S_3 Nanoplates Grown by Sulfurization. *2D Mater.* **2019**, *6* (3), No. 035029.
(70) Giannozzi, P.; Andreussi, O.; Brumme, T.; Bunau, O.; Nardelli, M. B.; Calandra, M.; Car, R.; Cavazzoni, C.; Ceresoli, D.; Cococcioni, M.; Colonna, N.; Carnimeo, I.; Dal Corso, A.; de Gironcoli, S.; Delugas, P.; DiStasio, R. A.; Ferretti, A.; Floris, A.; Fratesi, G.; Fugallo, G.; Gebauer, R.; Gerstmann, U.; Giustino, F.; Gorni, T.; Jia, J.; Kawamura, M.; Ko, H. Y.; Kokalj, A.; Küçükbenli, E.; Lazzeri, M.; Marsili, M.; Marzari, N.; Mauri, F.; Nguyen, N. L.; Nguyen, H. V.; Otero-de-la-Roza, A.; Paulatto, L.; Poncé, S.; Rocca, D.; Sabatini, R.; Santra, B.; Schlipf, M.; Seitsonen, A. P.; Smogunov, A.; Timrov, I.; Thonhauser, T.; Umari, P.; Vast, N.; Wu, X.; Baroni, S. Advanced Capabilities for Materials Modelling with Quantum Espresso. *J. Phys.: Condens. Matter* **2017**, *29* (46), No. 465901.

https://doi.org/10.1021/acsami.4c11537
ACS Appl. Mater. Interfaces 2024, 16, 54837−54846